Left Ventricular Chamber Shape During Vena Caval Occlusion: Improved MRI-based Measurement of the End-Systolic Pressure-Volume Relationship in Normal Sheep

Duc M. Giao[2,4,5], Yan Wang[3], Renan Rojas[2,4,5], Kiyoaki Takaba[2,4,5], Anusha Badathala[2,4,5], Kimberly A. Spaulding[2,4,5], Gilbert Soon[2,4,5], Yue Zhang[2,4,5], Vicky Y. Wang[2,4,5], Henrik Haraldsson[3], Jing Liu[3], David Saloner[3,5], Liang Ge[2,4,5], Julius M. Guccione[2,4,5], Arthur W. Wallace[1,2,5], and Mark B. Ratcliffe[2,4,5]

Departments of Anesthesia[1], Bioengineering[2], Radiology[3], and Surgery[4] of the University of California, San Francisco and the Veterans Affairs Medical Center, San Francisco, California[5]

Running Head: End-systolic Pressure Volume Relationship by Real-time MRI

Keywords: Left ventricle, Myocardial contractility, Pressure volume relationship, MRI, Left Ventricular Ellipticity

Text Word Count: 8308 words.

Corresponding Author: Mark B. Ratcliffe, MD, Surgical Services (112), Veterans Affairs Medical Center, 4150 Clement Street, San Francisco, California 94121. Telephone: (415) 221-4810. E-mail: Mark.Ratcliffe@va.gov

Abstract

The left ventricular (LV) end-systolic pressure volume relationship (ES; ESPVR) is the cornerstone of systolic LV function analysis. Recently, it became possible to measure 2D LV chamber shape during vena cava occlusion (VCO) with MRI. We used an improved level-set semi-automatic segmentation method (LSSM) to determine the effect of VCO on LV geometry, ES pressure area (PA) and ESPVR.

10 healthy adult sheep were anesthetized. LV pressure transducer and inferior vena cava (IVC) balloon catheter were percutaneously inserted. Ferumoxytol (0.125 ml/kg iv; AMAG Pharmaceuticals, Waltham, MA) was given to enhance blood pool contrast. LV pressure and 2D retrospectively-gated cine MRI of LV cross sections 25 (Apex), 50 (Mid) and 75% (Base) of the distance from the apex to the base of the LV were obtained during separate IVC balloon inflations (VCO). LV pressure was digitally filtered and LV chamber segmented with the LSSM. Cross sectional area, major and minor axes, major axis orientation, ESPAR and ESPVR were calculated.

The LSSM had excellent reliability. All cross sections became more elliptical during VCO. The orientation (angle) of each major axis relative to the anterior RV insertion shifted during VCO. However, the orientation remained toward the septum. There was chamber collapse (LV area < 0.25 cm^2) at the apical level during VCO (7 cases). ESPAR was non-linear at all levels. ESPVR was non-linear because of apical collapse.

In conclusion, MRI-based measurement of LV geometry, ESPAR and ESPVR during VCO is a valuable method that may lead to improved understanding of systolic LV function.

Word Count: 250 words

New and Noteworthy

Real-time MRI was used to continuously measure the LV PA relationship as loading conditions were transiently varied in anesthetized sheep. All three examined cross-sections became more elliptical during VCO. The ESPAR were non-linear at all three cross-sections. Chamber collapse at the apical level during VCO resulted in a non-linear ESPVR. The heart contracted in a non-concentric manner during VCO which could inform modeling studies and elucidate mechanisms underlying LV adaptations to sudden load changes.

Word Count: 74 words

Introduction

Left ventricular (LV) end-systolic pressure volume relationship (ESPVR) is considered the cornerstone of LV systolic function measurement (19). The ESPVR is widely used in cardiovascular preclinical research and development of pharmaceuticals and devices to quantify LV pump function, and has been proposed as an improved measurement of systolic heart failure (16).

The ESPVR is typically measured during transient vena cava occlusion (VCO) (12). Commonly used technologies for precise and rapid measurement of LV pressure (LVP) can be attained using high fidelity pressure catheters while that of LV volume (LVV) can be acquired by ultrasonic sonomicrometry transducers or the multi-electrode conductance catheter (1, 2, 13). Sonomicrometry requires surgical implantation of small ultrasonic transducer crystals on the LV wall that send sound signals to each other, and the transmit time between transducers allow for measurement of the signal distance between them. Pioneering work using sonomicrometry in healthy dogs by Tyson et al. demonstrated that both ventricular diameters (ie. major and anterior-posterior minor axis) decreased simultaneously during VCO (15, 22). Also using sonomicrometry, Olsen et al. found that the LV became more elliptical at large volumes and more spherical at small volumes during isovolumetric contraction, as LV deviation from sphericity was measured to be a linear function of LVV during both diastole and systole (14). However, this technique involves measurement of wall thickness that is usually problematic as the crystals are usually positioned at a single, arbitrary point on the LV wall, which has varying thickness from the valvular plane to the septum. Despite the new knowledge gained from the sonomicrometry measurement, clinical utility of this technique is hampered by its applicability for human subjects,

so the conductance catheter is the only practical technique for simultaneous acquisition of LVP and LVV in humans. The conductance catheter technique measures electrical conductance of blood in the LV, which is converted to blood pool volume using formulae that rely on a complex relationship between blood conductivity and electrical myocardial properties that are often difficult to accurately measure and personalize. In addition, this technique does not allow for geometric data of the LV to be obtained, and may not provide an accurate measurement when the LV collapses during VCO.

In the past, it has been unclear whether ESPVR is linear or nonlinear. The ESPVR, if linear, can be quantified by its slope known as the end-systolic elastance (E_{ES}) and a volume intercept at zero pressure (V_o) to define the position of ESPVR in the pressure-volume (PV) plane (20). E_{ES} thus serves as an important load-independent measure of myocardial contractility, which requires simultaneous measurement of LVP and LVV as loading conditions are varied. However, this linear ESPVR relationship gives rise to two problems. First, van der Velde et al. has described that the ESPVR exhibits nonlinearity and dependence on afterload, and hence does not serve as a perfect measure of load-independent LV contractility (23). And secondly, V_o derived from a linear ESPVR could lead to negative values at zero pressure, which is physiologically inaccurate as the LV can never attain negative blood volume.

Conventional cine magnetic resonance imaging (MRI) allows for excellent imaging at various cross sections of the LV slice-by-slice, but slow acquisition times do not enable continuous imaging of the LV during transient loading conditions and thus does not allow assessment of beat-by-beat changes in the LV PV relationship. Recently, Witschey and colleagues described a real time MRI based method to evaluate LV contractile function from continuous measurement of LV

PV loops, where 2D slice-derived LV area from level-set active contouring were matched with total LV volume using the cardiac cycle to assess PV relations (5, 28).

In our work, we used real-time MRI (RTMRI) to continuously measure LVP and LVV during transient loading conditions in anesthetized sheep. We used a semi-automatic level set algorithm together with enhanced contrast with Ferumoxytol to allow for rapid determination of slice-by-slice LV chamber geometry changes by assessing the ellipticity of the LV, major axis orientation angle, and segmental collapse and LV area segmentation for accurate pressure-area (PA) relations at apical, midventricular, and basal LV levels as loading conditions were varied. By imaging three segmental levels spanning the LV, we obtained the ESPVR using a modified Simpson's trapezoidal sum of the slice-derived ESPAR and derived key index of LV PV relationships such as E_{ES} and V_o. Using RTMRI, we tested the hypothesis that the slice-derived LV area assumes an elliptical shape during VCO, with non-uniform contraction in the septal-lateral direction, and apical segmental LV collapse which determines a non-linear ESPVR that has a positive volume intercept.

Methods

Overview

A flowchart illustrating the methodology used to determine real-time LV PV relationships from MRI is shown in **Figure 1**. Briefly, high resolution 2-dimensional (2D) RTMRI was performed along the short axis of the LV at apical, midventricular, and basal (25, 50, 75%) levels per sheep during transient loading conditions by VCO. Slice-by-slice LV chamber shape changes and LVA were determined by semi-automatic contouring of the real-time data set and synchronized with the LVP to obtain LV PA relations. LV PA relations were then used to calculate time-varying LV volume (LVV) and calibrated by surface fitting 3-dimensional (3D) cine MRI scans to assess load-independent measures of LV contractile function.

Animal Procedure

Sheep were treated under a protocol approved by the San Francisco VA Institutional Animal Care and Use Committee (IACUC), in compliance with the "Guide for the Care and Use of Laboratory Animals" prepared by the Institute of Laboratory Animal Resources, National Research Council. Sheep were sedated with ketamine (20mg/kg intravenous), anesthetized (Isoflurane 2.2% inhaled) and mechanically ventilated. The tip of a pressure catheter (SPC-350; Millar, Houston, TX) was immersed in water at 38°C for 12 hours prior to calibration and positioning in the LV and an 8 Fr balloon catheter was positioned in the inferior vena cava via femoral vessels using fluoroscopic guidance. Ferumoxytol (0.125 ml/kg IV over 1 hour; AMAG Pharmaceuticals, Waltham, MA) was given 1 hour prior to MRI (3). Metoprolol (5 mg) and atropine (1 mg) were also given intravenously immediately prior to MRI. Isoflurane was maintained at 2.2%; end-tidal CO_2 was

kept between 25 and 45 mm Hg; an infusion of neosynephrine was titrated to keep peak LV pressure at 90±5 mm Hg during cardiac MRI.

Cardiac Magnetic Resonance Imaging (cMRI)

Ten healthy, adult sheep underwent cardiac MRI. MRI imaging was performed on a 3T MRI scanner (Skyra; Seimens, Verlagen, Germany). Six cine long axis MR images that were 30° apart were first obtained and this set of baseline scans was used for LVV determination prior to VCO (21). Subsequently, LV pressure (LVP) and 2D cine real time MR images at three locations across the LV were then acquired during transient vena caval occlusion (VCO). The MR imaging parameters are summarized as follows: 2D multislice retrospectively-gated cine balanced steady-state free-precession acquisition with the following imaging parameters, TE = 1.34 ms, TR = 59.2 ms, acquisition matrix = 128 x 54, FOV = 178 x 260, slice thickness = 8 mm, pixel spacing = 2.0313 x 2.0313 mm. LVP acquisition (12 bit, 5K samples/ sec, ACQ16 and Ponemah 5.2, DSI, St. Paul, MN) started approximately 5 seconds before the start of the MRI acquisition as shown in **Figure 2**. 2D MR images were obtained at 25, 50 and 75% of the distance from the LV apex to valve plane with respiration suspended at end expiration.

Semi-automatic level-set segmentation

Level set-based segmentation method has been widely used for cardiovascular image segmentation (24, 26). In this study, a semi-automatic, active contour level set algorithm was used for segmentation of 2D cine MRI scans to obtain measurement of LV area (LVA) (27) and to fit an ellipse to assess LV shape changes. Specifically, the epicardium and endocardium including the papillary muscles, if present, of the LV at the first frame were manually contoured, while the contours for the subsequent frames were generated automatically using a shape constrained level

set method (27). When the contours determined by the level set algorithm extended into the right ventricular cavity, they were manually adjusted.

To validate the accuracy of the level set algorithm, manual segmentation was used as the ground-truth (4, 25) and Dice coefficient, commonly used for measuring the overlap between manual and automatic segmentation, was evaluated (29). Manual segmentation was performed in a blinded manner: two readers drew manual contours for 200 slices from all subjects (20 slices for each sheep case) by using a Matlab-based segmentation tool as shown in **Figure 3A**. The intra- and inter-observer variability were investigated by drawing manual contours two times in 3 cases and comparing the semi-automatic segmentation with manual contours from two readers using Dice similarity coefficient (**Figure 3B**).

LV Hemodynamics Measurement

Hemodynamic parameters including cycle length, ES interval, and LVP were measured at baseline conditions, which started five beats before the start of VCO to the start of the VCO, and compared to conditions during preload reduction. Cycle length represented the time of a full cardiac cycle and was measured from one end-diastole time point to the next end-diastole time point (ED-ED) time interval, while ES interval was defined as the time from ED to ES to indicate the time for contraction. LVP attained from LV pressure catheter was also measured at each LV segment to assess regional pressure differences at both baseline and preload reduction conditions.

LV Geometry Analysis: Real time MRI

After performing the proposed level set segmentation, the LV area of the cardiac cycle was delineated by multiplying the number of the pixels within the contour by the pixel area. An ellipse was then fitted to the epicardial contours at each time point including papillary muscle if present,

from which the major and minor axis ratio (MajMinR) and major axis orientation angle with respect to the septal point on the right ventricle (RV) were derived and used to quantify LV shape changes during VCO as illustrated in **Figure 3C**. Major axis orientation angle was used as a measure of the degree of the LV major axis twisting away from the vertical axis defined by the RV septal insertion point and also as the direction of contraction, with positive values indicating LV contraction in the septal-lateral direction and negative values indicating contraction in the anterior-posterior direction (movie in Supplementary Material). Additionally, we obtained the time points at which the LV segment collapsed, as determined when LVA < 0.25 cm^2. In instances where the LV collapsed, the axis and angle data were excluded. Two different time points (before and during) of the VCO at mid-ventricle are shown to illustrate the LV shape and area changes in **Figure 4**.

ESPVR analysis: Real time MRI

In order to construct the ESPVR using both the real time MRI and pressure data, a multi-step framework was proposed as described below. All analyses codes were developed using customized software written in C# (Visual Studio 2017, Microsoft, Redmond, WA) using Matlab routines (.NET assembly using Matlab Compiler, Mathworks).

1. **Baseline LVV quantification**: LV endocardial and epicardial borders were manually contoured from the baseline long-axis images and LVV at end-diastole (ED) and end-systole (ES) were subsequently calculated using MeVisLab (18). Baseline LVV measurements were indexed to body surface area (6) to the power of 1.5 (7).
2. **Pressure analysis:** LVP was filtered with an in-line analog filter (BNC Low Pass Filter, Crystek, Fort Myers, FL) during acquisition and post-processed with a digital constrained

least Pth-norm IIR filter (Matlab R2016b, Mathworks, Natick, MA). After filtering, LVP was calibrated using pressure acquired immediately prior to MRI acquisition as shown in **Figure 2B**. The derivative of the LV pressure (dP/dt) was also calculated to align with the LVA data.

3. **LVP and LVA alignment:** LVA was initially aligned to the region of noise on the unfiltered LVP trace. dP/dt and LVA peaks were detected and beats were created with peak maximum dP/dt aligned with peak LVA. This scheme of alignment was chosen to obtain optimal LV PA loops (**Appendix Figure 1**). The ESPAR was determined using an iterative regression approach similar to that used for conductance ESPVR calculation (11).
4. **Estimation of ES LVV for ESPVR**: LV volume at ES was determined with the following:

$$LVV(P)_{ES} = \sum_{i=1}^{5} \frac{1}{2} \left(LVA(P)_i + LVA_{i+1}\right)\left(LVDist_{i+1} - LVDist_i\right) + LVV_{ES,0} \qquad (1)$$

where $LVA(P)_i$ is LV cross-sectional area with i ranges from 1 (LV apex) to 5 (LV valve plane), $LVDist_i$ is the distance of the real time MRI short-axis slices from the LV apex. Note that $LVDist_{5=ValvePlane}$ is assumed to move toward the apex in line with sonomicrometry data obtained in conscious dogs during VCO (22). $LVV_{ES,0}$ is the baseline ES volume calculated from step 1 and is assumed to be constant during the VCO. Subsequent points on the ESPVR are generated using $LVA(P)_i$ at LVP range between 50 and 90 mmHg with a 5 mmHg step change.

Statistical analysis

All values are expressed as mean ± standard error of the mean. The significance level was set at $p<0.05$.

Multivariate mixed effect analyses (Proc Mixed, SAS version 9.2, SAS Institute Inc., Cary, NC) were performed to examine the changes in LV shape during VCO. Individual sheep were included as a random effect (10). The Bonferroni method was used to correct for multiple comparisons.

Results

Semi-automatic level set method

Semi-automatic level set algorithm allowed for quantification of LV volume from real-time MRI during rapidly changing loading conditions. Level set based segmentation was automatic in 7 of 10 sheep data sets and required minor parameter modifications in the remaining 3 of 10 data sets.

The intra-observer variability from the two readers were 0.54% and 0.88%. The Dice similarity coefficient was used for inter-observer variability measurement between level set segmentation comparing with manual results from two readers and determined to be 87.31%±2.51% and 88.13%±3.43% respectively, thus showing achieving a high segmentation accuracy as shown in **Figure 3B**. A representative LV area vs time plot calculated from the active contours is shown in **Figure 4**.

Hemodynamic parameters at baseline and during preload reduction

We compared hemodynamic measurements of the LV at baseline conditions during preload reduction. All average measurements are reported in **Table 1**. The length of the cardiac cycle and ES interval had small differences across the apical, midventricular, and basal segments at both baseline and during VCO. Comparing the parameters at baseline and during VCO at all three LV segments, the cycle length did not change but the ES intervals were shortened by an average of 0.03 sec, indicating an increase in the rate of contraction. LVP was observably lower in the apical segment (88.6 $\pm$ 1.60 mm Hg) compared to that of the midventricular and basal segments (94.8 $\pm$ 1.34 and 95.1 $\pm$ 1.40 mm Hg respectively) at baseline, however, it was relatively uniform at all three LV segments during VCO.

Ellipticity of LV

Average baseline LV morphology measurements including LV area, major axis, minor axis, axis ratio, and major axis orientation angle measurements are reported in **Table 1**. As expected, LV area, major axis, and minor axis lengths increased as the slice moved from the apical to the midventricular to the basal segment. Conversely, axis ratios increased as the slice moved from the basal to midventricular to the apical segment, confirming that the LV is more spherical at the basal segment and more elliptical at the apical segment. Major axis orientation angle was greatest at the midventricular segment with an average angle of 51.2° while the basal and apical segments had average angles of 29.9° and 13.7° respectively. Separate mixed-effects linear models were used to investigate the changes in the major axis orientation level at each of the three LV segments at the start until the end of VCO. An analysis of variance (ANOVA) test was run on the slopes of the linear fits reported in **Table 2** comparing the three level segments and were not found to be significant. However, positive angle values at all three segments indicate that the LV contracts in the septal-lateral direction at both baseline and during VCO.

We sought to examine whether the shape of the LV changes at the apical, midventricular, and basal segments at ES during reduced loading conditions. **Figure 5** shows changes in major axis length, minor axis length, axis ratio (MajMinR), and major axis orientation angle with respect to the septal point on the RV for a representative sheep case at mid-ventricle. We fitted an overall mixed-effects linear model on MajMinR at each LV segment and found that the increase was best fit by a linear function, $MajMinR_{Level} = \beta_o + \beta_1 X. \beta_1$ slope terms were 0.0084 ($p<0.05$), 0.0072 ($p<0.05$), and 0.0085 ($p<0.05$) at the apical, midventricular, and basal segments respectively,

suggesting that LV was initially spherical and gradually became elliptical as LVP decreased at all three LV segments.

We observed that the LV globally transforms from an initially more spherical shape to an elliptical shape as the LVP decreases until LVP = 48.73 mm Hg, an average pressure which LVA determined from active contours then becomes less than 0.25 cm^2. At this low pressure, the LV wall collapses with bowing of the interventricular septum into the LV cavity. A subset of the linear effects model for apical slices reveals that the LVA = 0 at an average LVP = 52.27 mm Hg, suggesting that the apical segment collapses at a higher pressure than the midventricular (LVP = 12.02 mm Hg) and basal segments (LVP = 8.39 mm Hg).

LV collapse at the apical segment during VCO was observed in 7 of the 10 cases (27 beats). At this point, the axis lengths were too small that the level-set algorithm was unable to detect the difference between the LV intercavitary space from the RV and surrounding tissue, thus LV area, axis, and angle measurements were set to equal 0 and excluded from the data set. Representative plots of LV area, major axis, and minor axis are shown for an apical slice of one sheep case, where specific time points after time = 15 sec indicate LV collapse as LV area, and both major and minor axis lengths are measured to be 0 in **Figure 6**.

RTMRI based ESPAR

We aimed to determine slice-by-slice derived ESPAR by combining LVA determined from level set algorithm and LVP from LV pressure catheter. As described by Witschey and coworkers, the use of balloon catheter occlusion allows the estimation of load-independent measures of LV function at each slice position (5, 28). LVA decreases over a wide range of pressure decrement (120 mmHg – 50 mmHg) as represented in **Figure 4.** Time-varying LV PA loops at apical,

midventricular, and basal sections for one animal are shown in **Figure 7A-C**. As expected, a rightward shift in the PA loops was observed as the slice moved from the apical to the midventricular to basal segment. Similar results were observed in PA loops in all animals. We then investigated the slope of ESPAR and the LVA at zero pressure, A_o, by observing PA relations during preload reduction. ESPAR slope and area intercept for all animals at 25, 50 and 75% LV levels are illustrated in **Figure 8A, Figure 8B,** and **Appendix Table 1.** At low EDP, we observed that the slope of ESPAR appeared to increase, suggesting a curvilinear PA relationship. A mixed-effect linear model was used to investigate the nonlinear relationship between LVP and LVA (Eq. 1: $LVP = \beta_o + \beta_1 LVA + \beta_2 LVA^2$; where β_o = A_o, β_1 and β_2 are the regression coefficients). The results suggested a nonlinear relationship for ESPAR β_2= -0.500 ($p<0.001$), β_1=9.209 ($p<0.001$), β_0=48.73 ($p<0.001$) for this cohort of sheep.

ESPVR Calculation

MRI-based ESPVR was calculated using modified Simpson's rule (Eq. 1) for all animals from the linear-fitted ESPAR instead of the quadratic function-fitted ESPAR which provided a small β_2 term. Using the linear ESPVR calculation method devised by Suga and Sagawa (19, 20), we evaluated the slope of ESPVR known as end-systolic elastance E_{ES} and the LVV at zero pressure V_o by observing PV relations during transient LV volume reduction. E_{ES} and V_o for all animals are shown in **Figure 9A, Figure 9B** and **Appendix Table 2.** Overall, we found E_{ES} = 2.31$\pm$ 3.1 mm Hg/mL and V_o = -13.61 $\pm$ 2.41 mL. However, based on our observations that the slope of the ESPVR increased at low EDP and EDV and implications from LV collapse of the apical segment, we contrasted this linear ESPVR approximation method using a mixed-effect linear model ($LVP = \beta_o + \beta_1 LVV + \beta_2 LVV^2$; where β_o = V_o, and β_1 and β_2 are the regression

coefficients) to evaluate the nonlinearity of the ESPVR, with the restriction that ESPAR points < 0 were restricted to LVA = 0, as the LVA cannot attain negative area values. The results indicated that the ESPVR is nonlinear: β_2=0.0414 (p<0.001), β_1=0.349 (p<0.001), β_0=18.12 (p<0.001) and load-dependent especially at low EDP, giving rise to a curvilinearity concave to the volume axis. An example of a representative MRI-based ESPVR of one animal is shown in **Figure 9C**. Similar results were observed in the entire cohort of sheep.

Discussion

The principal finding of the study is that the LV contracts in the septal-lateral direction, and gradually becomes more elliptical at all three examined LV levels as LVP is decreased during VCO, leading to LV collapse first at the apical segment. Non-uniform sequential collapse of the LV thus has implications in determining whether the ESPVR is linear or non-linear.

Semi-automatic active contouring

Our use of Ferumoxytol allowed for impressive visualization and contrast of the LV to supplement our active contour segmentation using level set. Ferumoxytol is an ultrasmall supramagnetic iron oxide serving as an alternative to gadolinium based contrast agents. It is a blood pool agent with a long blood half-life, about 12 hours, providing excellent contrast-to-noise ratio between the blood pool and surrounding tissue, a feature beneficial for contouring (8).

In order to calculate LV structural and functional indices, delineation of the boundaries of the LV chambers is essential. In this study, the level set based method was used to quantify LV geometry. The resultant LV contours demonstrated that the semi-automatic method was comparable to manual segmentation. The computation time for semi-automatic segmentation was less than 10 seconds per slice, although more powerful computing could greatly shorten the processing time.

Hemodynamics Changes during VCO

Beta blockers, metoprolol and atropine, were given to abolish autonomic response to VCO. Cardiac cycle length and ES intervals were determined at all three LV levels to determine whether blood flow to the LV was adequately blocked via VCO. ES interval differences across the three LV segments were small and not significant. Beat effect was defined as the progression of the

beat number during VCO and was found to have a highly significant effect on ES interval ($p<0.001$). There was no beat effect on cycle length so we concluded that the sheep were adequately blocked. We anticipate that the decreased ES interval observed is due to the decreased amount of blood ejected during preload reduction. Lower baseline LVP at the apical segment compared to the midventricular and basal segments suggest a regional pressure drop at the LV apex, possibly due to the lower blood volume present for ejection. However, we attribute slight differences in measurement of cycle length, ES interval, and LVP at the three LV levels to inaccuracies in our measurement technique using MRI, as it takes a series of scans and then looks at the triggering signal to reconstruct the images, which includes a time delay between the data collected at each slice.

LV Geometry Changes during VCO

The increasing major to minor axis ratio at mid-ventricle scans suggests that the LV was initially more spherical but became elliptical as LV pressure decreased. Therefore, the LV does not contract in a concentric fashion. This twisting and torsion motion of the LV is fundamental to measurement of contractility and improves our understanding of LV contraction models for ventricular modeling (9, 17). Our findings revealed that ellipticity of the LV was related linearly at ES to LVP at the all three examined segments, as the chamber transforms from an initially more spherical shape to become elliptical as loading conditions are reduced. As defined by our level set algorithm, positive major axis orientation angle values indicate that the LV contracts in the septal-lateral direction during VCO. Varying major axis orientation angle values were measured at the three LV segments, suggesting non-uniform torsion of the LV during normal contraction with greatest twisting at the midventricular segment. Even though this method of

characterizing ventricular geometry is a simplification of the complex LV geometry and contraction, it offers a rapid assessment of the dynamic shape changes of the LV over a large physiological range of LV pressures and insight into the non-uniform shape changes at ED and ES.

Gradual LV geometric changes to assume an elliptical shape during VCO have major implications in our interpretation of the ESPVR, discussed more thoroughly further on, due to sequential LV collapse of apical slices at LVP = 48.73 mm Hg. As stated before, the LV cannot assume negative blood volume at LVP = 0 mm Hg during and after the LV wall collapses. The ESPVR can be analyzed in both a linear (20) and nonlinear (23) fashion to derive LV myocardial systolic performance. We have determined that the ESPVR should be interpreted as nonlinear, described in further detail in the following section, where no negative LV areas obtained from active contour segmentations and no base descent were included in the calculation of the ESPVR. More specifically, we observed that the apical LV collapses at a higher pressure than the midventricular and basal segments, so the apical area stops decreasing at area = 0 and therefore the obtained ESPVR curve then becomes curvilinear. Even when the ESPAR plots appear nearly linear as could be argued in the PA loops presented in **Figure 7A-C**, the ESPVR can be nonlinear because of segmental LV collapse.

RTMRI ESPVR

We found that the slice-by-slice derived ESPAR was best fit by a quadratic function, and although the regression coefficients β_1 and β_2 in $LVP = \beta_o + \beta_1 LVA + \beta_2 LVA^2$ were small, they were statistically significant. Previous work has shown that the ESPVR exhibits nonlinearity and dependence on afterload (23). Similarly, we observed that the ESPVR was nonlinear and load-

dependent especially at low EDP. In most of the studies reported previously, the ESPVR is suggested to be approximated by a linear regression with end-systolic elastance and volume intercept as indicators of load-independent myocardial contractility. Again, this linear calculation leads to negative V_o values which contradicts current physiological understanding of how the LV cannot attain negative blood volume at zero pressure. However, in the majority of these studies (20, 22), the pressure and volume ranges over which the data were collected did not span large enough physiological ranges that would reveal the nonlinear character of the ESPVR. Close inspection of the ESPVR data points generally showed a slight curvilinearity concave with respect to the volume axis, which is particularly discernable at low EDP and EDV. This nonlinear relationship takes into account physiologic considerations which require that V_o cannot attain negative values, which are obtained when linear extrapolation of ESPVR is performed as shown. The data presented in this study can be used to tune/optimize mathematical models of active contraction.

Limitations

There are several limitations in the present study. First, clinical utility assessing load-independent LV systolic function in patients necessitates for a method to noninvasively assess LV pressure and continuous measurement of LV volume. RTMRI addresses the second of these challenges, however assessment of LV pressure requires the insertion of a pressure catheter into the LV long axis. Also, varying loading conditions were made possible using balloon occluding catheters, which serves well in preclinical research but is by no means feasible in patients.

Additionally, LV ESPVR and shape change analysis must also take into careful consideration the effects of right-sided filling pressures, pericardial pressures, and ventricular interdependence. It

has been described previously that LV minor axis diameter changes during preload reduction is not only a LV measurement, but is also dependent on biventricular volume changes through direct ventricular interaction (15).

RTMRI serves as an efficient preclinical tool to rapidly assess LV PV relations as loading conditions were varied, but improvements should be aimed at deriving more accurate means to attain slice-by-slice ESPAR from LVP and MRI-based LVA to calculate ESPVR. Our current technique consists of 6-8 images per beat, which we apply a spline fit to interpolate the area points prior to matching the area and pressure data. Thus, in some cases, the corners of the PA loops are rounded and do not have perfect regions of isovolumetric contraction and relaxation, giving rise to potentially up to an % error of 10-15% (ie. 2 cm^2 out of an average LVA of 14 cm^2). To reduce such error, future studies should experiment with different fits for the area data such as using a more rectangular shape to allow for more accurate PA loops. Additional efforts should be aimed at improving the imaging technique to provide more than 6-8 images per beat so more data points could be interpolated to form more precise PA loops. Extraction of PA data for ESPAR during VCO of the sheep is constrained by the lowest achievable LVP of approximately 40 mm Hg, so PA relations cannot be obtained at low EDP and EDV. Despite these limitations, we believe that RTMRI holds the potential to allow for not only rapid but accurate assessment of LV contractility and geometry.

Clinical Implications

RTMRI is a powerful tool that permits rapid assessment and quantification of regional LV shape changes and systolic function. Our data suggest that LV geometry changes and sequential collapse during VCO have clinical implications in our evaluation of the ESPVR and use of its slope, end-

systolic elastance E_{ES}, as a global measure of LV contractile function. We have found that the heart contracts in a non-concentric manner during preload reduction, improving our understanding of regional LV shape changes during cardiac conditions such as hypovolemic shock, when there is a sudden and significant circulatory volume drop as was seen during VCO. Our study not only serves as an appropriate model of the LV geometry changes during abrupt pressure and volume changes but also key regional PV relations in understanding regional myocardial contractility. Our findings are an appropriate adjunct for areas of investigation of surgical technologies such as left-ventricular assist devices (LVADs) in assisting cardiac circulation to either partially or completely replace LV pump function in patients with a failing LV. Understanding the non-uniform fashion in which the LV contracts and the nonlinearity of the ESPVR may therefore be useful in developing LVADs that are sensitive to LV pressure and volume during physiological conditions that require varying amounts of blood pumped.

Conclusion and future directions

In summary, we used RTMRI to assess LV hemodynamic and geometry changes and measure LV contractility using real-time MRI-based PV relations. This method has potential application to study cardiac disease by assessing regional contractile function in preclinical setting.

Future work improving peripheral pressure measurements to noninvasively measure LV pressure while loading conditions are varied will need to be achieved through less invasive means, possibly through pharmacologic agents. Further work using RTMRI should be focused on assessing the LV geometric changes and the ESPVR in animals after myocardial infarction as a model for cardiac disease. Additionally, assessment of MRI-derived end-diastolic pressure-volume relationship would be vital in characterizing diastolic filling at specified loading pressures and

passive ventricular properties including chamber geometry, wall thickness, passive material properties of the myocardial wall. Future studies should also consider three dimensional (3D) RTMRI methods to more accurately evaluate global LV shape changes for multi-dimensional analysis and contractile function.

Acknowledgements

The authors would like to acknowledge the staff from the animal facility at the San Francisco Veterans Affairs Medical Center for their help facilitating the animal procedures.

Grants

This study was supported by National Heart, Lung and Blood Institute Grant R01-HL-084431 (M. Ratcliffe).

Disclosures

No conflicts of interest, financial or otherwise, are declared by the author(s).

Author Contributions

A.W.W. and M.B.R. conceived and designed the research study; D.M.G., R.R., K.T., A.B., K.A.S., G.S., Y.Z., H.H., and M.B.R. performed experiments; D.M.G., Y.W., Y.Z., V.Y.W., and M.B.R. analyzed data; D.M.G., Y.Z., V.Y.W., and M.B.R. interpreted results of experiments; D.M.G., Y.W., Y.Z., and V.Y.W. prepared figures; D.M.G., Y.W., V.Y.W., and M.B.R. drafted manuscript; D.M.G., Y.W., K.A.S., Y.Z., V.Y.W., J.M.G., A.W.W., and M.B.R. edited and revised manuscript; J.L., D.S., L.G., J.M.G., A.W.W., and M.B.R. approved final version of manuscript.

Appendix

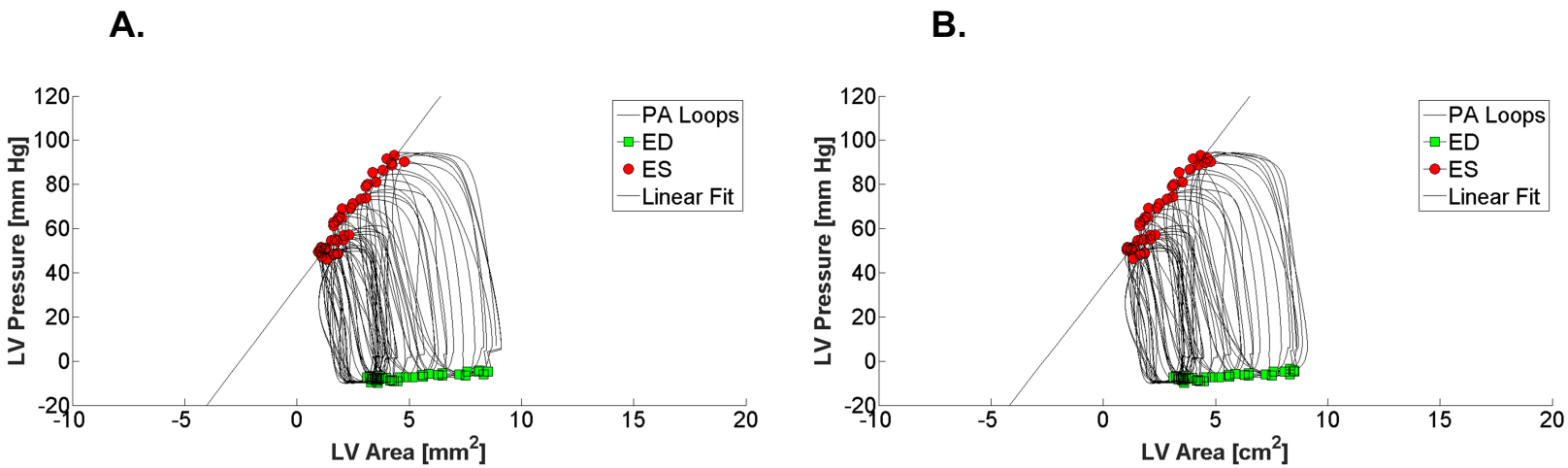

Appendix Figure 1: Alignment using max + dLVP/dt and max LV area was initially chosen because of the perception that beat shape was more appropriate. In retrospect, there is little effect between this (A) and 0.25 max + dLVP/dt and max LV area (B).

	ESPAR Slope [mm Hg/cm^2]			**A_o [cm^2]**		
Animal #	**Apex**	**Mid**	**Base**	**Apex**	**Mid**	**Base**
1	4.18	26.3	11.0	-18.5	-0.858	-1.63
2	11.6	23.4	9.07	-4.87	-0.543	-2.80
3	9.67	8.08	6.68	-4.52	-0.395	-2.28
4	18.0	16.6	8.13	-2.97	-0.820	-3.69
5	13.3	13.5	4.75	-3.63	-2.61	-12.5
6	9.28	7.80	6.84	-4.25	-4.04	-1.50
7	10.8	26.0	19.9	-5.29	-0.675	-1.07
8	8.67	13.1	7.86	-9.20	-4.03	-3.32
9	13.1	15.0	5.54	-4.55	-1.69	-7.75
10	8.51	14.1	10.4	-9.48	-2.30	-2.46
Mean $\pm$ SEM	10.7 $\pm$ 1.16	16.4 $\pm$ 2.13	9.02 $\pm$ 1.36	-6.73 $\pm$ 1.48	-2.15 $\pm$ 4.59	-3.90 $\pm$ 1.12

Appendix Table 1: Slope and volume intercept of ESPAR at three LV levels derived from RTMRI-based analysis.

Animal #	**E_{ES} [mm Hg/mL]**	**V_o [mL]**
1	3.26	-8.21
2	1.87	-16.0
3	1.38	-18.4
4	2.35	-12.7
5	1.74	-29.2
6	1.57	-15.4
7	2.51	-11.2
8	1.96	-16.6
9	1.79	-6.64
10	4.70	-7.73
Mean $\pm$ SEM	2.31$\pm$3.10	-13.6$\pm$2.41

Appendix Table 2: End-systolic elastance E_{ES} (slope) and volume-axis intercept (V_o) estimated from the ESPVR indexed to basal surface volume $(BSA)^{1.5}$.

References

1. **Applegate RJ, Cheng CP, and Little WC**. Simultaneous conductance catheter and dimension assessment of left ventricle volume in the intact animal. *Circulation* 81: 638-648, 1990.

2. **Baan J, van der Velde ET, de Bruin HG, Smeenk GJ, Koops J, van Dijk AD, Temmerman D, Senden J, and Buis B**. Continuous measurement of left ventricular volume in animals and humans by conductance catheter. *Circulation* 70: 812-823, 1984.

3. **Bashir MR, Bhatti L, Marin D, and Nelson RC**. Emerging applications for ferumoxytol as a contrast agent in MRI. *Journal of Magnetic Resonance Imaging* 41: 884-898, 2014.

4. **Chen Y, Navarro L, Wang Y, and Courbebaisse G**. Segmentation of the thrombus of giant intracranial aneurysms from CT angiography scans with lattice Boltzmann method. *Medical Image Analysis* 18: 1-8, 2014.

5. **Contijoch F, Rogers K, Rears H, Shahid M, Kellman P, Gorman J, Gorman RC, Yushkevich P, Zado ES, Supple GE, Marchlinski FE, Witschey WRT, and Han Y**. Quantification of Left Ventricular Function With Premature Ventricular Complexes Reveals Variable Hemodynamics. *Circ Arrhythm Electrophysiol* 9: e003520, 2016.

6. **Dubois E**. The estimation of the surface area of the body. In: *Basal metabolism in health and disease*, edited by Dubois E. Philadelphia, PA: Lea and Febiger, 1936, p. 125-144.

7. **Gutgesell HP, and Rembold CM**. Growth of the human heart relative to body surface area. *The American Journal of Cardiology* 65: 662-668, 1990.

8. **Hope MD, Hope TA, Zhu C, Faraji F, Haraldsson H, Ordovas KG, and Saloner D**. Vascular Imaging With Ferumoxytol as a Contrast Agent. *American Journal of Roentgenology* 205: W366-W373, 2015.

9. **Ibrahim E-SH**. Myocardial tagging by Cardiovascular Magnetic Resonance: evolution of techniques--pulse sequences, analysis algorithms, and applications. *Journal of Cardiovascular Magnetic Resonance* 13: 36, 2011.

10. **Kleinbaum DG**. *Applied regression analysis and other multivariable methods*. Belmont: Thomson Brooks/Cole Publishing, 2008.

11. **Kono A, Maughan W, Sunagawa K, Hamilton K, Sagawa K, and Weisfeldt M**. The use of left ventricular end-ejection pressure and peak pressure in the estimation of the end-systolic pressure-volume relationship. *Circulation* 65: 988-997, 1984.

12. **Little WC, Cheng CP, Mumma M, Igarashi Y, Vinten-Johansen J, and Johnston WE**. Comparison of measures of left ventricular contractile performance derived from pressure-volume loops in conscious dogs. *Circulation* 80: 1378-1387, 1989.

13. **Mirsky I, Tajimi T, and Peterson KL**. The development of the entire end-systolic pressure-volume and ejection fraction-afterload relations: a new concept of systolic myocardial stiffness. *Circulation* 76: 343-356, 1987.

14. **Olsen CO, Rankin JS, Arentzen CE, Ring WS, McHale PA, and Anderson RW**. The deformational characteristics of the left ventricle in the conscious dog. *Circulation Research* 49: 843-855, 1981.

15. **Olsen CO, Van Trigt P, and Rankin JS**. Dynamic geometry of the intact left ventricle. *Circ Res* 52: 85-104, 1983.

16. **Sagawa K**. The end-systolic pressure-volume relation of the ventricle: definition, modifications and clinical use. *Circulation* 63: 1223-1227, 1981.

17. **Simpson RM, Keegan J, and Firmin DN**. MR assessment of regional myocardial mechanics. *Journal of Magnetic Resonance Imaging* 37: 576-599, 2012.

18. **Soleimani M, Khazalpour M, Cheng G, Zhang Z, Acevedo-Bolton G, Saloner DA, Mishra R, Wallace AW, Guccione JM, Ge L, and Ratcliffe MB**. Moderate mitral regurgitation accelerates left ventricular remodeling after posterolateral myocardial infarction. *Ann Thorac Surg* 92: 1614-1620, 2011.

19. **Suga H, and Sagawa K**. Instantaneous Pressure-Volume Relationships and Their Ratio in the Excised, Supported Canine Left Ventricle. *Circulation Research* 35: 117-126, 1974.

20. **Suga H, Sagawa K, and Shoukas AA**. Load Independence of the Instantaneous Pressure-Volume Ratio of the Canine Left Ventricle and Effects of Epinephrine and Heart Rate on the Ratio. *Circulation Research* 32: 314-322, 1973.

21. **Turk G, and O'Brien JF**. Shape transformation using variational implicit functions. In: *Proceedings of the 26th annual conference on Computer graphics and interactive techniques - SIGGRAPH '99*ACM Press, 1999.

22. **Tyson GS, Maier GW, Olsen CO, Davis JW, and Rankin JS**. Pericardial influences on ventricular filling in the conscious dog. An analysis based on pericardial pressure. *Circulation Research* 54: 173-184, 1984.

23. **van der Velde ET, Burkhoff D, Steendijk P, Karsdon J, Sagawa K, and Baan J**. Nonlinearity and load sensitivity of end-systolic pressure-volume relation of canine left ventricle in vivo. *Circulation* 83: 315-327, 1991.

24. **Wang Y, Courbebaisse G, and Zhu YM**. Segmentation of giant cerebral aneurysms using a multilevel object detection scheme based on lattice Boltzmann method. In: *2011 IEEE International Conference on Signal Processing, Communications and Computing (ICSPCC)*IEEE, 2011.

25. **Wang Y, Navarro L, Zhang Y, Kao E, Zhu Y, and Courbebaisse G**. Intracranial Aneurysm Phantom Segmentation Using a 4D Lattice Boltzmann Method. *Computing in Science & Engineering* 19: 56-67, 2017.

26. **Wang Y, Seguro F, Kao E, Zhang Y, Faraji F, Zhu C, Haraldsson H, Hope M, Saloner D, and Liu J**. Segmentation of lumen and outer wall of abdominal aortic aneurysms from 3D black-blood MRI with a registration based geodesic active contour model. *Medical Image Analysis* 40: 1-10, 2017.

27. **Wang Y, Zhang Y, Navarro L, Eker OF, Corredor Jerez RA, Chen Y, Zhu Y, and Courbebaisse G**. Multilevel segmentation of intracranial aneurysms in CT angiography images. *Medical Physics* 43: 1777-1786, 2016.

28. **Witschey WRT, Contijoch F, McGarvey JR, Ferrari VA, Hansen MS, Lee ME, Takebayashi S, Aoki C, Chirinos JA, Yushkevich PA, Gorman JH, Pilla JJ, and Gorman RC**. Real-Time Magnetic Resonance Imaging Technique for Determining Left Ventricle Pressure-Volume Loops. *The Annals of Thoracic Surgery* 97: 1597-1603, 2014.

29. **Yan W**. Study of the lattice Boltzmann method application to cerebral aneurysm segmentation. INSA de Lyon, 2014.

Figure 1.

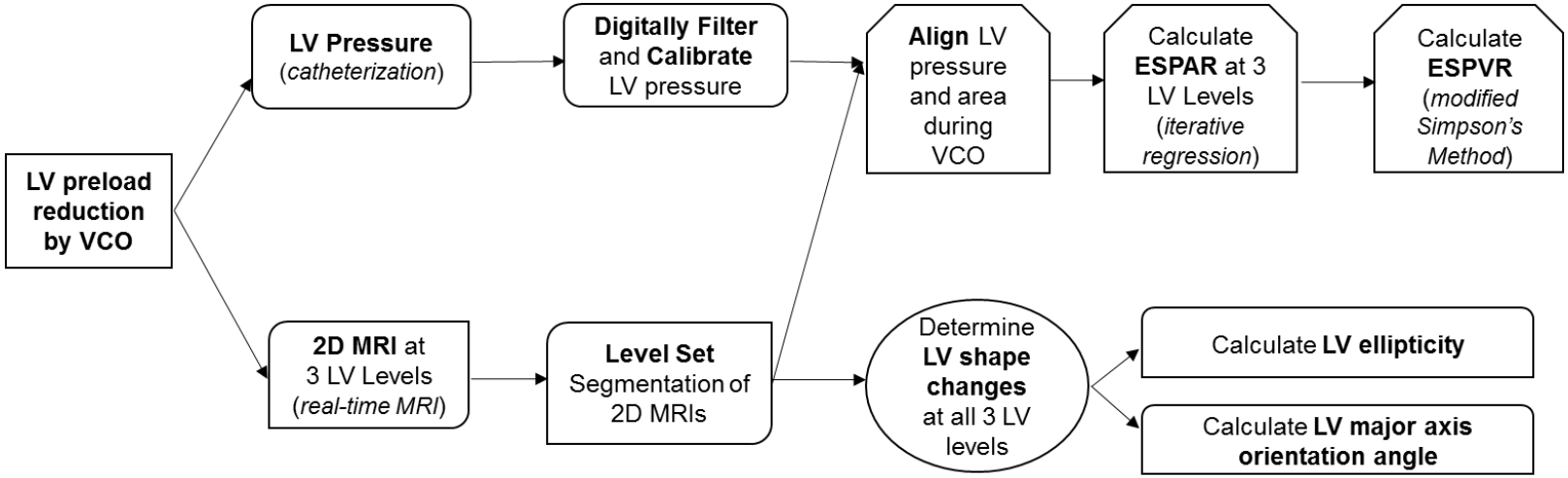

Figure 1: A flowchart illustrating the overall methodology designed to derive subject-specific ESPVR from RTMRI and pressure catheter measurement.

Figure 2.

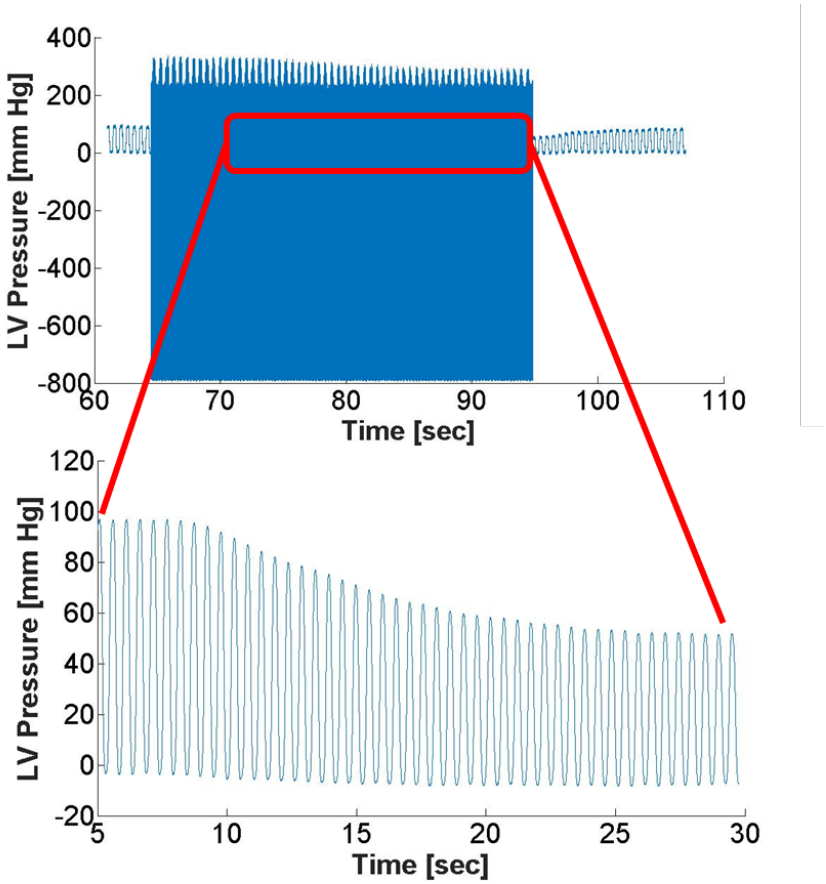

Figure 2: Raw pressure data with noise prior to digital filtering and calibration (top) with the insert showing filtered and calibrated LV pressure during the selected VCO range.

Figure 3.

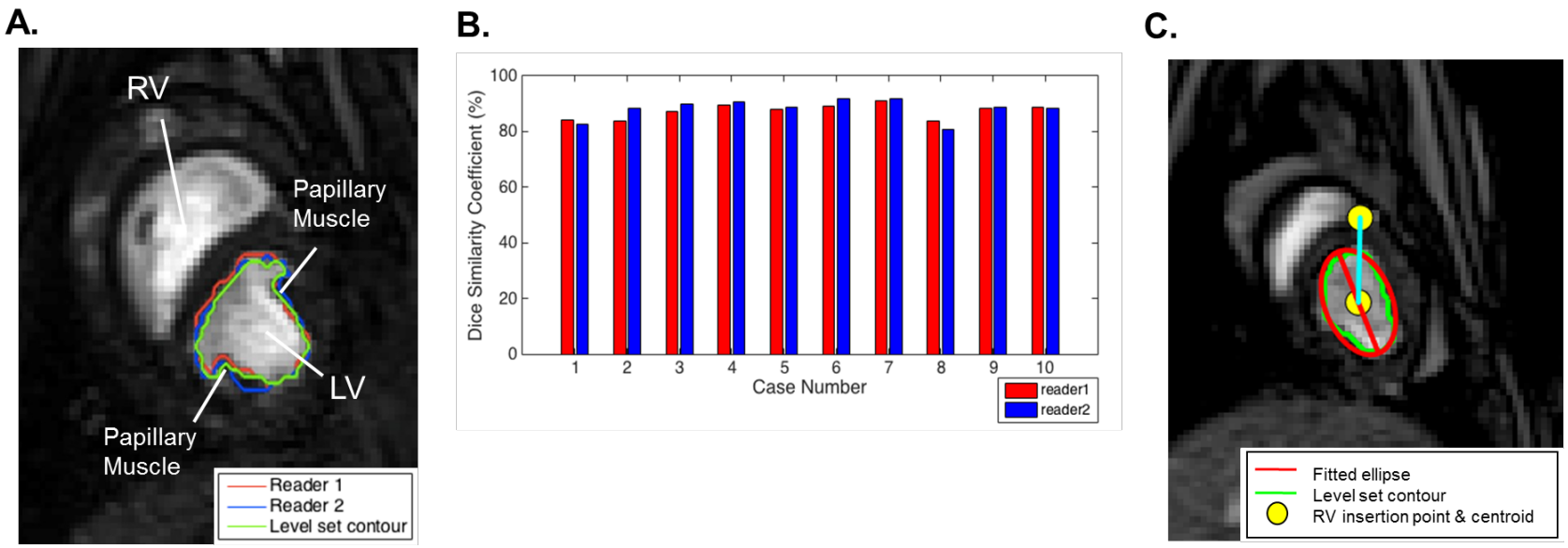

Figure 3: **(A)** Representative midventricular short-axis image of the LV showing level set and manual contours. Green = automatic contouring, Red = manual contour reader 1, Blue = manual contour reader 2. **(B)** Dice similarity coefficient for all 10 cases. (**C**) Representative midventricular short-axis image of the LV overlaid with automatic contours and fitted ellipse for quantifying major/minor axis length and major axis orientation angle as surrogate measurement of LV shape change. Red = fitted ellipse. Green = automatic contouring. Yellow circle = RV insertion point and centroid of ellipse. Movie is included in the Supplementary Material.

Figure 4.

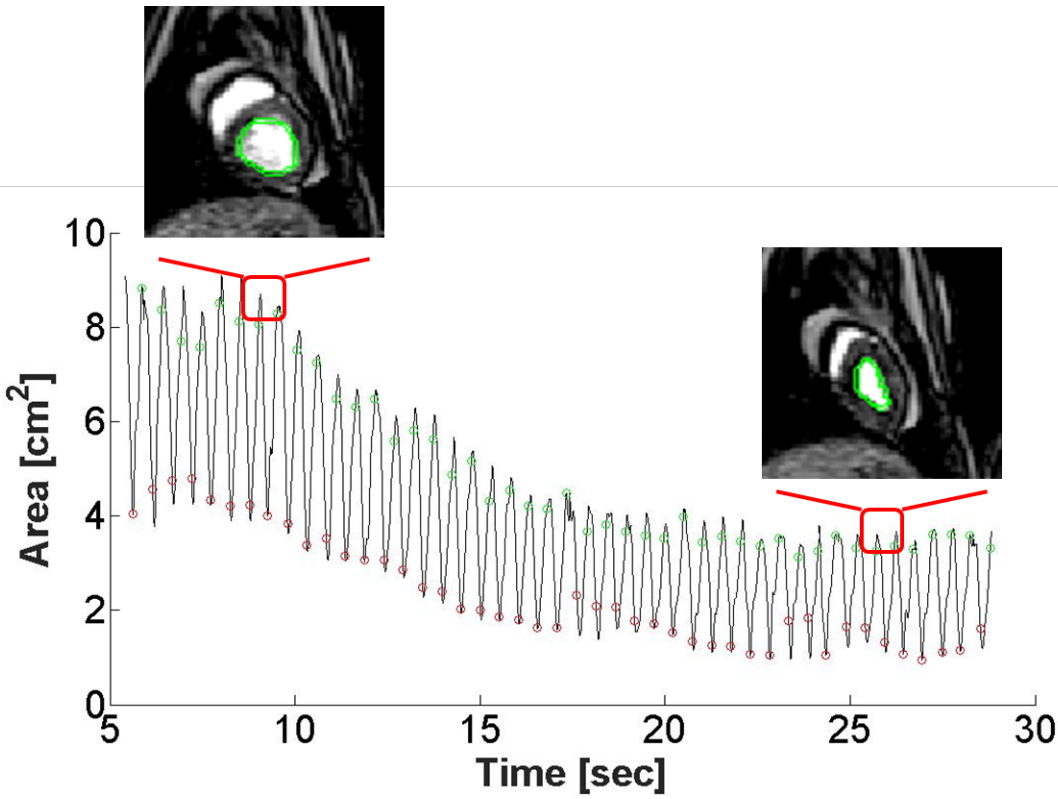

Figure 4: LV Area plot calculated by the level set algorithm with representative midventricular short-axis images of the LV before VCO and during VCO starting at t = 10 sec. Green makers = end-diastole (ED), Red markers = end-systole (ES).

Figure 5.

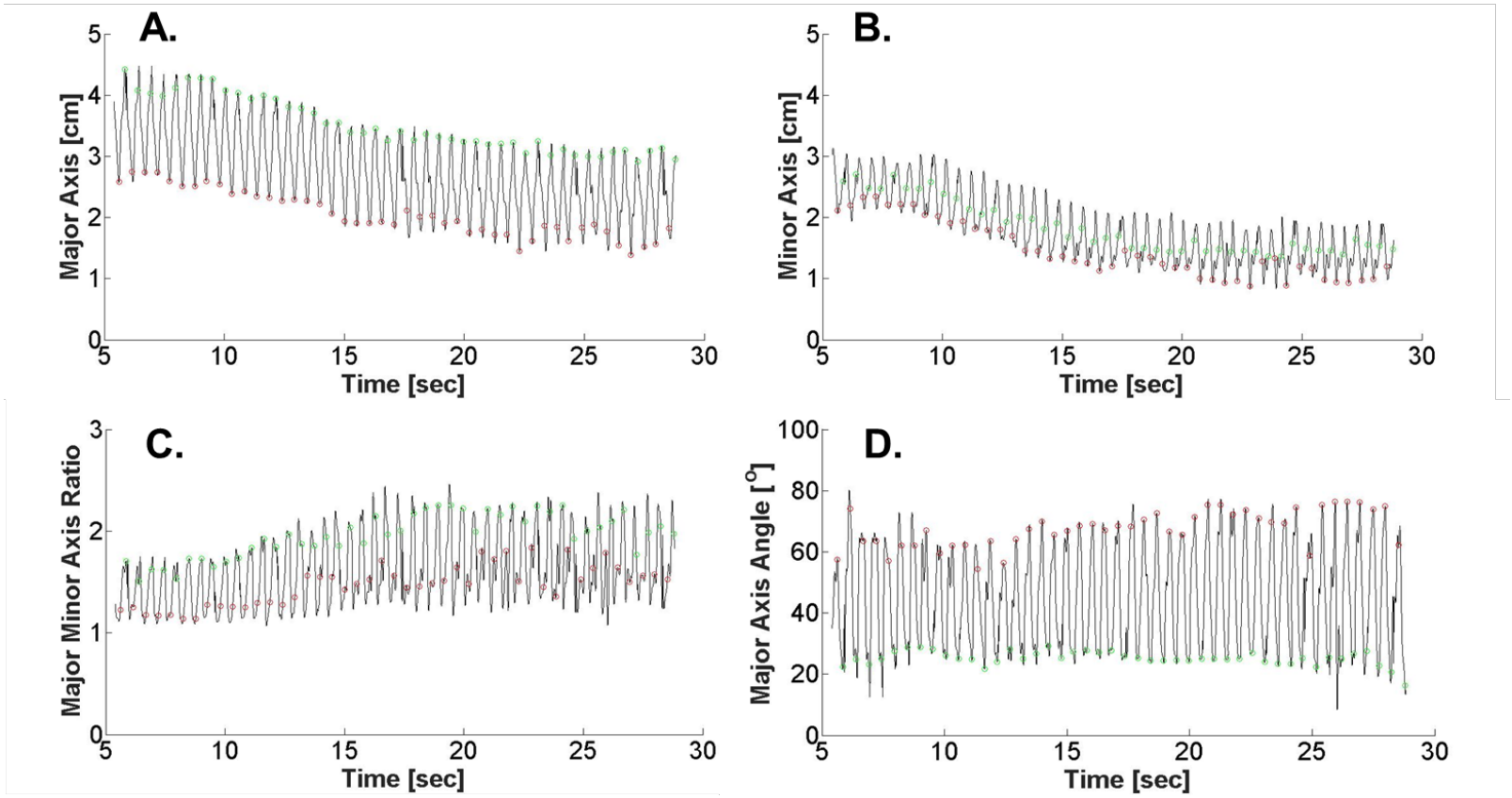

Figure 5: Changes in LV geometry before and during VCO. Shape changes were quantified by 4 indicators calculated from the fitted ellipse:**(A)** Major Axis length, **(B)** Minor Axis length, **(C)** Major to Minor Axis Ratio (MajMinR), and **(D)** Major Axis Orientation Angle. Green makers = end-diastole (ED), Red markers = end-systole (ES).

Figure 6.

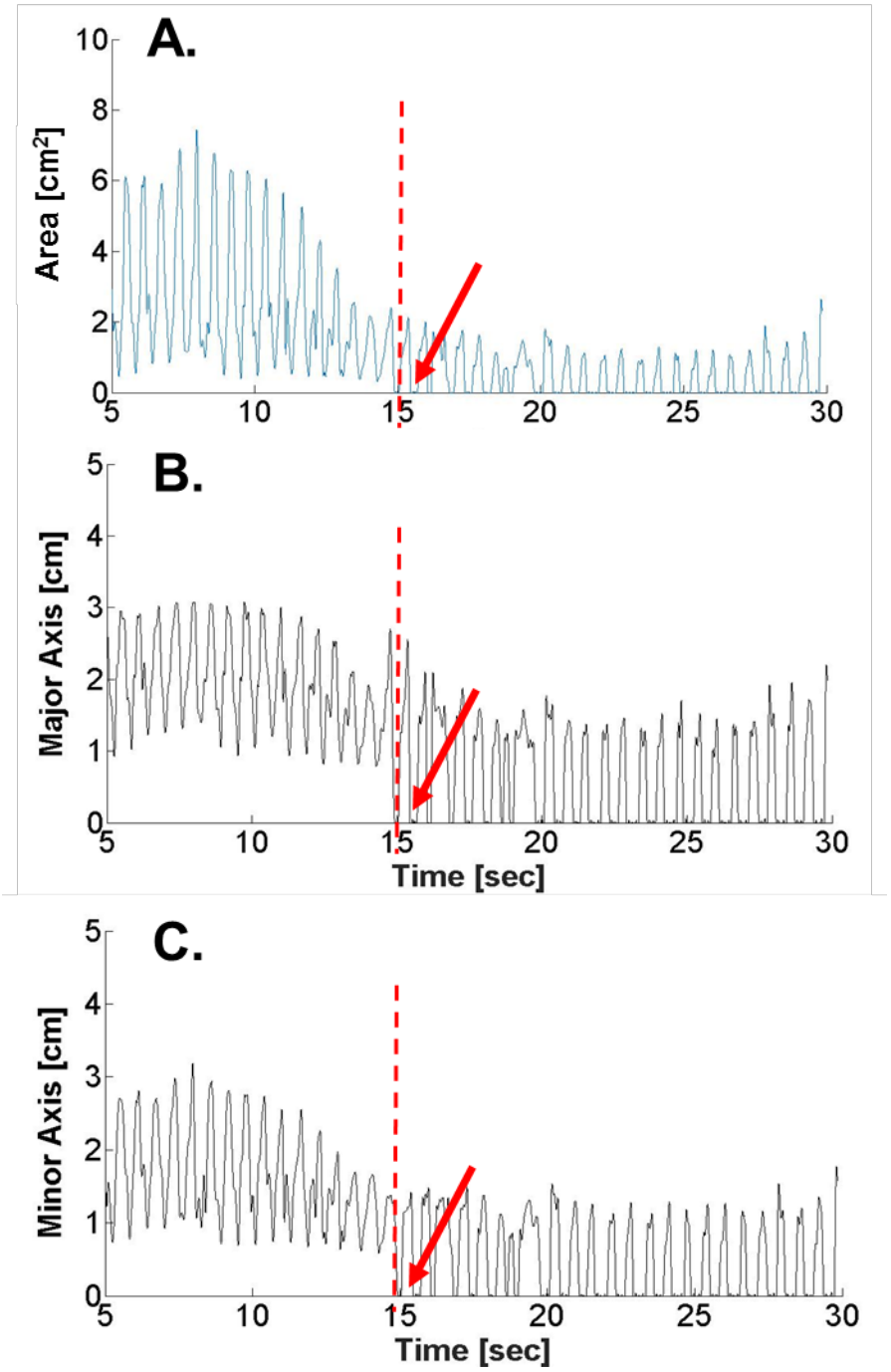

Figure 6: Plots of LV Apical Area **(A)**, Major Axis length **(B)**, and Minor Axis length **(C)** of a case showing segmental collapse where LVA < 0.25 cm^2 after time = 15 sec as indicated by a red arrow.

Figure 7.

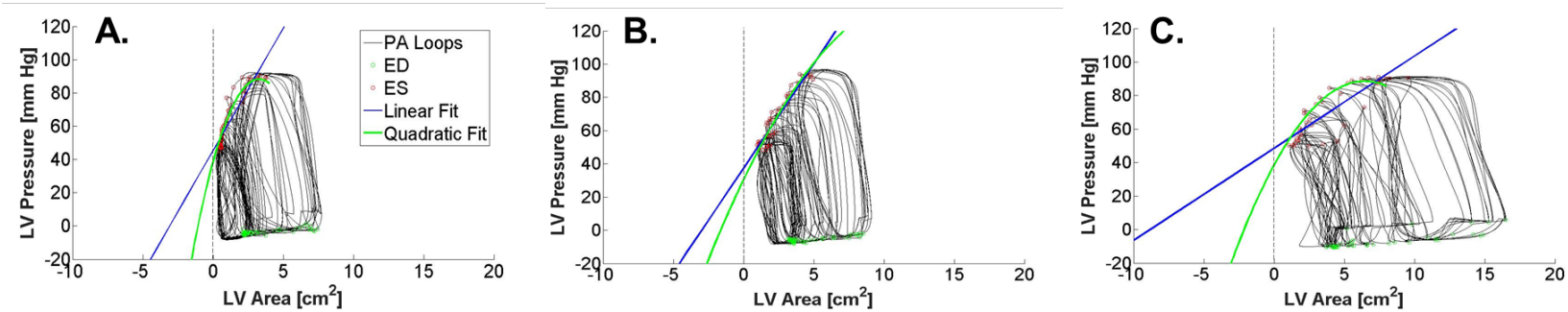

Figure 7: Representative LVP-area (LVPA) loops derived from the level set algorithm and pressure measurements along with fitted ESPAR at apex **(A)**, mid-ventricle **(B)**, and base **(C)** during VCO. The ESPAR was fitted with a linear function (blue) and a quadratic function (green) for comparison. The vertical dashed line represents collapse of the LV to zero volume.

Figure 8.

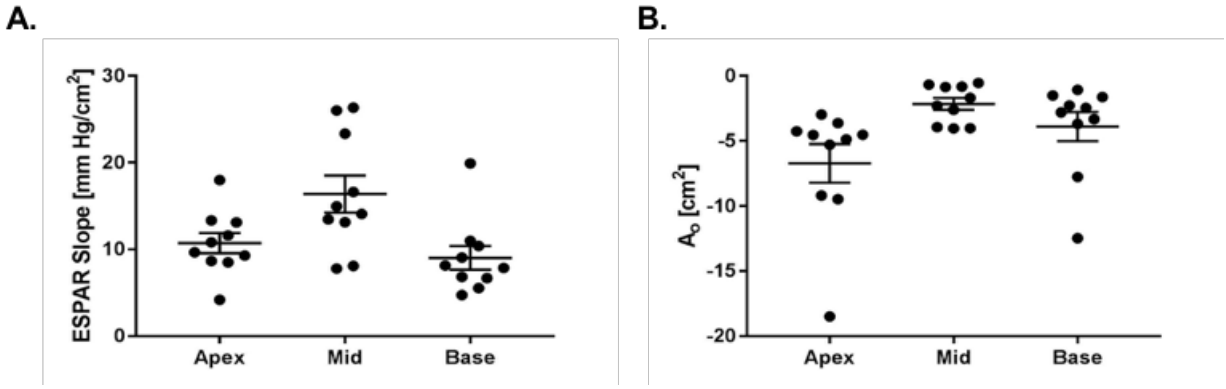

Figure 8: Slope of ESPAR **(A)** and LV area intercept A_o **(B)** at apex, mid, and base LV levels for all animals indexed to basal surface volume.

Figure 9.

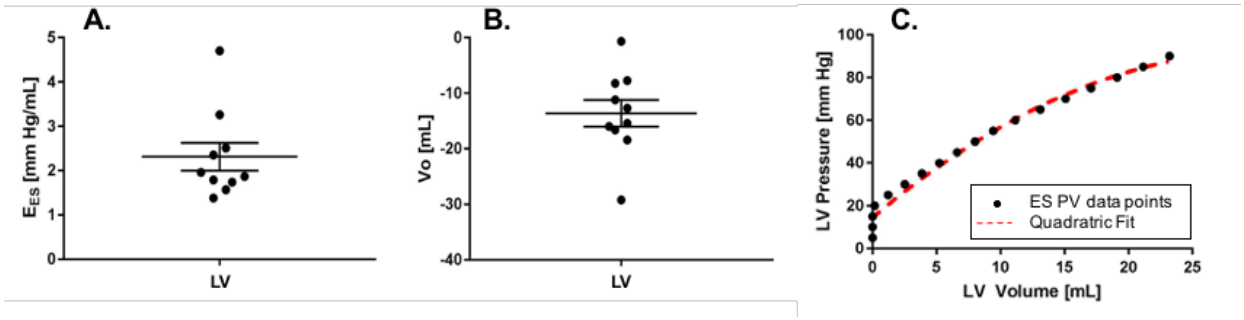

Figure 9: End-systolic elastance E_{ES} **(A)** and volume intercept V_o **(B)** of ESPVR indexed to basal surface volume. Representative ESPVR with a quadratic fit in red dashed line **(C).**

Figure Legends

Figure 1: A flowchart illustrating the overall methodology designed to derive subject-specific ESPVR from RTMRI and pressure catheter measurement.

Figure 2: Raw pressure data with noise prior to digital filtering and calibration (top) with the insert showing filtered and calibrated LV pressure during the selected VCO range.

Figure 3: **(A)** Representative midventricular short-axis image of the LV showing level set and manual contours. Green = automatic contouring, Red = manual contour reader 1, Blue = manual contour reader 2. **(B)** Dice similarity coefficient for all 10 cases. (**C**) Representative midventricular short-axis image of the LV overlaid with automatic contours and fitted ellipse for quantifying major/minor axis length and major axis orientation angle as surrogate measurement of LV shape change. Red = fitted ellipse. Green = automatic contouring. Yellow circle = RV insertion point and centroid of ellipse. Movie is included in the Supplementary Material.

Figure 4: LV Area plot calculated by the level set algorithm with representative midventricular short-axis images of the LV before VCO and during VCO starting at t = 10 sec. Green makers = end-diastole (ED), Red markers = end-systole (ES).

Figure 5: Changes in LV geometry before and during VCO. Shape changes were quantified by 4 indicators calculated from the fitted ellipse:**(A)** Major Axis length, **(B)** Minor Axis length, **(C)** Major to Minor Axis Ratio (MajMinR), and **(D)** Major Axis Orientation Angle. Green makers = end-diastole (ED), Red markers = end-systole (ES).

Figure 6: Plots of LV Apical Area **(A)**, Major Axis length **(B)**, and Minor Axis length **(C)** of a case showing segmental collapse where LVA < 0.25 cm^2 after time = 15 sec as indicated by a red arrow.

Figure 7: Representative LVP-area (LVPA) loops derived from the level set algorithm and pressure measurements along with fitted ESPAR at apex **(A)**, mid-ventricle **(B)**, and base **(C)** during VCO. The ESPAR was fitted with a linear function (blue) and a quadratic function (green) for comparison. The vertical dashed line represents collapse of the LV to zero volume.

Figure 8: Slope of ESPAR **(A)** and LV area intercept A_o **(B)** at apex, mid, and base LV levels for all animals indexed to basal surface volume.

Figure 9: End-systolic elastance E_{ES} **(A)** and volume intercept V_o **(B)** of ESPVR indexed to basal surface volume. Representative ESPVR with a quadratic fit in red dashed line **(C).**

Appendix Figure 1: Alignment using max + dLVP/dt and max LV area was initially chosen because of the perception that beat shape was more appropriate. In retrospect, there is little effect between this **(A)** and 0.25 max + dLVP/dt and max LV area **(B)**.

Tables

	All VCOs (n=30)	**Apex (n=10)**	**Mid (n=10)**	**Base (n=10)**	**Significance***
Cycle Length [sec]	0.637±0.007	0.631 ± 0.008	0.640 ± 0.012	0.641± 0.014	NS
ES Interval [sec]	0.255±0.003	0.261 ± 0.005	0.246 ± 0.005	0.257 ± 0.005	1, 3
LV Pressure at ES [mm Hg]	92.9±0.9	88.6 ± 1.6	95.1 ± 1.4	94.8 ± 1.3	2, 3
LV Area at ES [cm^2]	5.43±0.25	2.53 ± 0.156	4.55 ± 0.181	9.15 ± 0.323	1, 2, 3
LV Major Axis at ES [cm]	2.77±0.06	1.99 ± 0.0601	2.637 ± 0.0573	3.66 ± 0.0627	1, 2, 3
LV Minor Axis at ES [cm]	2.37±0.06	1.63 ± 0.0622	2.27 ± 0.0456	3.20 ± 0.0576	1, 2, 3
LV Axis Ratio at ES	1.19±0.01	1.26 ± 0.0307	1.16 ± 0.0150	1.15 ± 0.0129	2, 3
Major Axis Orientation Angle at ES [^{o}]	31.7±3.7	13.7 ± 7.46	51.2 ± 5.67	29.9 ± 4.74	1, 2, 3

Table 1: Baseline cycle length, end-systolic (ES) interval, LV pressure and area, and major and minor axis, axis ratio and axis angle at ES for all VCO data and at three LV levels. *NS: not significant, 1: Base vs Mid ($p<0.05$), 2: Base vs Apex ($p<0.05$), 3: Mid vs Apex ($p<0.05$).

	All VCOs (n=30)	**Apex (n=10)**	**Mid (n=10)**	**Base (n=10)**	**Significance***
Cycle Length [sec/ beat]	-0.0038±0.0005	-0.0027±0.0008	-0.0043±0.0011	-0.0042±0.0006	1
ES Interval [sec/ beat]	-0.0024±0.0004	-0.0035±0.0009	-0.0018±0.0008	-0.0020±0.0004	1
LV Pressure at ES [mm Hg/ beat]	-2.26±0.11	-2.32±0.19	-2.23±0.21	-2.22±0.18	1
LV Area at ES [cm^2/ beat]	-0.13±0.02	-0.08±0.02	-0.11±0.01	-0.21±0.04	1,2
LV Major Axis at ES [cm/ beat]	-0.038±0.003	-0.033±0.008	-0.040±0.004	-0.043±0.0058	1
LV Minor Axis at ES [cm/ beat]	-0.042±0.004	-0.033±0.009	-0.041±0.004	-0.050±0.008	1
LV Axis Ratio at ES	0.0080±0.0017	0.0084±0.0041	0.0072±0.0020	0.0085±0.0026	1
Major Axis Orientation Angle at ES [^{o}/ beat]	-0.19±0.28	-1.04±0.46	-0.34±0.54	0.81±0.27	1,2

Table 2: Slope of cycle length, end-systolic (ES) interval, LV pressure and area, and major and minor axis, axis ration and axis angle at ES vs VCO beat for all VCO data and at three LV levels. *1: All VCO variables vs beat ($p<0.05$), 2: Base vs Apex ($p<0.05$).

Table Legends

Table 1: Baseline cycle length, end-systolic (ES) interval, LV pressure and area, and major and minor axis, axis ratio and axis angle at ES for all VCO data and at three LV levels. *NS: not significant, 1: Base vs Mid ($p<0.05$), 2: Base vs Apex ($p<0.05$), 3: Mid vs Apex ($p<0.05$).

Table 2: Slope of cycle length, end-systolic (ES) interval, LV pressure and area, and major and minor axis, axis ration and axis angle at ES vs VCO beat for all VCO data and at three LV levels. *1: All VCO variables vs beat ($p<0.05$), 2: Base vs Apex ($p<0.05$).

Appendix Table 1: Slope and volume intercept of ESPAR at three LV levels derived from RTMRI-based analysis.

Appendix Table 2: End-systolic elastance E_{ES} (slope) and volume-axis intercept (V_o) estimated from the ESPVR indexed to basal surface volume $(BSA)^{1.5}$.